Nanoscale

PAPER

View Article Online
View Journal | View Issue

Cite this: *Nanoscale*, 2025, **17**, 22315

Two-terminal analog memory comprising self-assembled monolayers of edge-fused porphyrin oligomers

Xinkai Qiu,[a] Jie-Ren Deng,[b] G. Andrew D. Briggs,[a] Harry L. Anderson *[b] and James O. Thomas *[a,c]

Received 30th June 2025,
Accepted 6th September 2025

DOI: 10.1039/d5nr02773j

rsc.li/nanoscale

The study of molecular electronic devices displaying hysteresis, non-volatility, and analog switching in their current–voltage characteristics not only reveals fundamental information on electron transfer, but also provides interesting candidates for next-generation computing paradigms. In this work we report on the charge-transport properties of a family of self-assembled monolayer junctions formed from edge-fused porphyrin oligomers (monomer, dimer and trimer). We show that hysteresis emerges as molecular length increases, and that ON–OFF ratios between high and low conductance states reach over 200 for edge-fused porphyrin trimers. By applying voltage sweeps, the junction conductance can be modulated to a series of intermediate conductance states, between the high and low conductance states, that are stable over hour timescales at room temperature.

Introduction

Molecular electronic devices have been shown to function as sensors, switches, transistors, and diodes, with the active component comprised of anything from a micrometer-thick film down to a single isolated molecule.[1] A common method of fabricating molecular devices is to form self-assembled monolayer (SAM) junctions. In these structures, electrons are transported between two macroscopic metallic electrodes *via* a layer of single molecules, ensuring a close relationship between the molecular structure and device properties, while the many parallel transport pathways minimize reproducibility issues associated with contacting an individual molecule. Computing paradigms with the potential to supersede complementary metal–oxide–semiconductor (CMOS) technology, such as neuromorphic computing, have generated significant research interest in devices that display memristor-like behavior (*i.e.*, hysteresis and non-volatility[2]), as they allow for low-power operation and in-memory computation.[3,4] This interest extends to molecular electronic devices,[5–7] including SAMs,[8–10] with a diverse range of mechanisms identified as leading to hysteresis in charge transport.

In this work, we study the charge transport properties of SAM junctions in which the molecular layer is comprised of edge-fused porphyrin oligomers of varying lengths. From the families of porphyrin oligomers for which single-molecule conductance has been measured, which also includes singly-linked[11] and butadiyne-linked porphyrins,[12,13] edge-fused oligomers display the smallest conductance attenuation with molecular length, attributed to larger inter-porphyrin electronic coupling and consequent reduction in energy-level spacings.[12,14] In addition to their high conductance, and prompting this investigation, it has been discovered that edge-fused oligomers switch between high- and low-conductance states in single-molecule junctions (SMJs).[14,15] We show that the SAM junctions also display switchable conductance states, however instead of the rapid stochastic switching behavior observed for SMJs, in SAM junctions, the high and low conductance states are smoothly connected by unipolar hysteresis loops. The different conductance states are separated by a factor of several hundred and are stable for up to 20 hours at room temperature. Furthermore, we show that these memristive junctions can be tuned to a range of intermediate conductance states, using a controlled series of switching operations, which is a property of interest for analog computing applications.[5,16]

[a]*Department of Materials, University of Oxford, 16 Parks Road, Oxford, OX1 3PH, UK*
[b]*Department of Chemistry, Chemistry Research Laboratory, University of Oxford, Oxford, OX1 3TA, UK. E-mail: harry.anderson@chem.ox.ac.uk*
[c]*School of Physical and Chemical Sciences, Queen Mary University of London, London, E1 4NS, UK. E-mail: j.o.thomas@qmul.ac.uk*

Results and discussion

Formation of SAMs

SAMs of **P1**, **FP2** and **FP3** (chemical structures are shown in Fig. 1a) were formed by immersing freshly prepared, ultra-

smooth template-stripped gold substrates (Au^{TS}) in toluene solutions of the porphyrin derivatives for 24 hours (see Experimental section for the fabrication of SAMs). The synthesis of **P1** is presented in the SI, and the synthesis of **FP2** and **FP3** has been reported previously.[12] The weak interaction between acetyl thioester anchor groups and the Au surface, combined with favorable molecular packing in the SAM, drives initial physisorption of the molecules. This is followed by the deprotection of acetyl thioesters at the molecule-Au interface and chemisorption, *i.e.*, the formation of S–Au bonds. The acetyl thioesters at the top interface remain protected, as depicted in Fig. 1b and demonstrated by the X-ray photoelectron spectroscopy (XPS) results discussed below.[17–20] We estimated the respective layer thicknesses of 13.7 Å for **P1**, 14.7 Å for **FP2** and 15.9 Å for **FP3** using XPS, as summarized in Table S2. The packing of the bulky molecules in their respective SAMs yields large tilt angles of 56° for **P1**, 63° for **FP2** and 67° for **FP3**, defined with respect to the surface normal and calculated from the SAM thicknesses and the molecular length (from DFT optimized structures, see Fig. S13). We calculate packing densities of 1.3×10^{13} molecules per cm^2 for **P1**, 1.1×10^{13} molecules per cm^2 for both **FP2** and **FP3** (Table S3), an order of magnitude lower than SAMs of alkanethiols on Au, which typically produce a tilt angle between 14–18° and a packing density of 5×10^{14} molecules per cm^2.[2,21,22] The surface morphology measured by atomic force microscopy (AFM) did not show vacancies in the SAMs (Fig. S6), and the roughnesses were similar to a bare Au^{TS} substrate (Table S4), suggesting the molecules form densely packed monolayers despite their bulky structures. XPS spectra of the S 2p region show S–C peaks that correspond to the protected acetyl thioesters (at 163.6 eV for S $2p_{3/2}$ and 164.7 eV for S $2p_{1/2}$) and deprotected acetyl thioesters, *i.e.*, thiolates (at 162.1 eV for S $2p_{3/2}$ and 163.3 eV for S $2p_{1/2}$). A peak area ratio of 1.2–1.3 between the protected and deprotected S signals in all three SAMs confirmed the formation of S–Au bonds at the molecule-Au interface, while the acetyl thioesters at the other end of the molecules were unaltered, as observed previously.[20] The attenuation of the deprotected S signal through the SAMs may account for a smaller peak area for the thiolate signals. The surface composition is also corroborated by an increased surface hydrophilicity of the SAMs in comparison to bare Au^{TS} substrate (Table S5). In the XPS spectra, the presence of a N–C/N=C peak (401.1 eV, Fig. S4) in the N 1s region and a Zn peak (1021.9 eV, Fig. S3) in the Zn 2p region that correspond to the porphyrin moiety, and a C=O peak (289.4 eV, Fig. S3) that corresponds to the acetyl thioester group further confirmed that anchoring groups away from the gold-molecule interface remain intact after SAM formation.

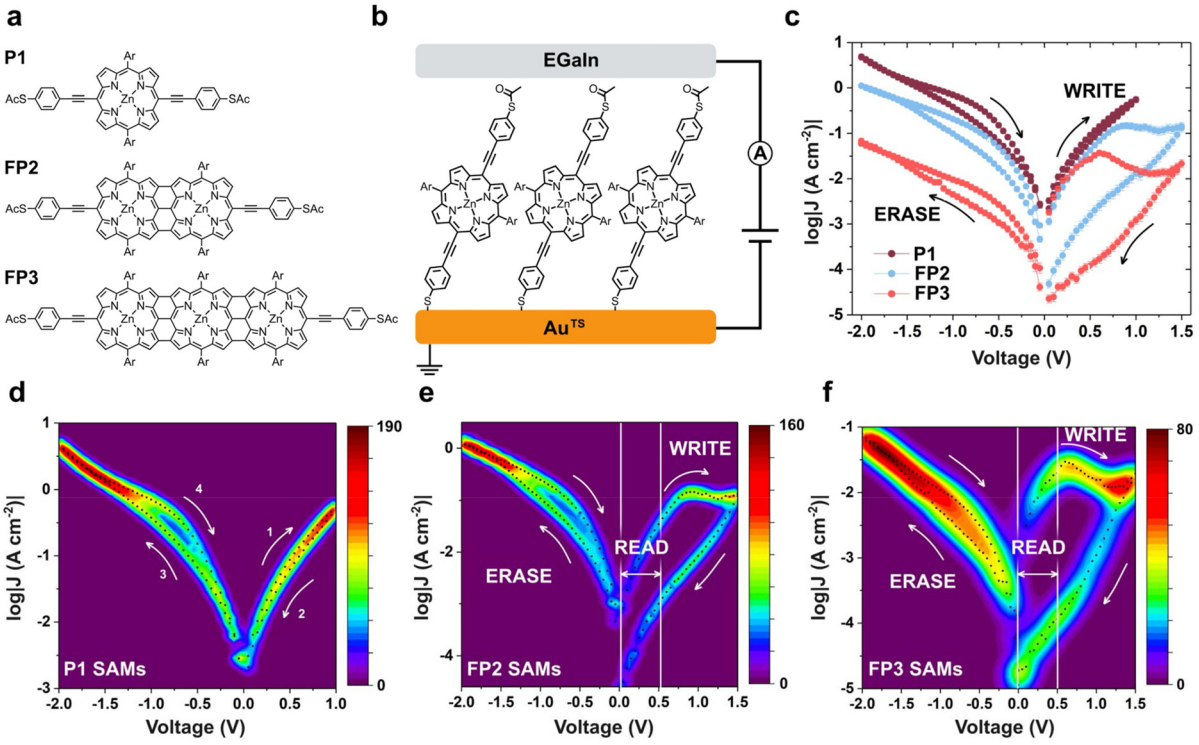

Fig. 1 Characterization of the charge-transport properties of the SAMs of fused porphyrin oligomers. (a) Chemical structures of molecules: **P1**, **FP2**, and **FP3**. Ar denotes an aryl group that increases solubility, Ar: 3,5-bis(trihexylsilyl)phenyl. (b) Schematic showing the structure of the Au^{TS}/SAM//EGaIn junctions; '/' denotes a chemisorbed interface and '//' denotes a physisorbed interface. Here, only the SAM of **P1** is shown for simplicity. (c) Plots of log|*J*| *versus* voltage for Au^{TS}/**P1**//EGaIn junctions and Au^{TS}/**FP***n* (*n* = 2, 3)//EGaIn junctions. In (c) and in (d–f) arrows and numbers show the direction and the order of applied bias (the same for three SAMs) and WRITE, ERASE, and READ operations are defined in the text. Error bars represent standard deviations. (d–f) Heat maps of log|*J*| *versus* voltage for Au^{TS}/**P1**//EGaIn (d), Au^{TS}/**FP2**//EGaIn junctions (e), and Au^{TS}/**FP3**//EGaIn junctions (f). Black dots represent the Gaussian means of log|*J*| at each voltage (see Experimental section).

Charge-transport characterization

We characterized the charge-transport properties of the SAMs by contacting them with sharp tips of eutectic Ga–In (EGaIn)[23] to form junctions with the structure: Au^{TS}/SAM//EGaIn, where '/' denotes interfaces defined by chemisorption and '//' by physisorption and the SAM being **P1**, **FP2** or **FP3**. In our devices the Au^{TS} substrate is grounded, and the bias voltage is applied to the EGaIn tip. Despite their low packing densities, the SAMs are robust against high biases: the junctions comprising the SAMs of **P1** short at ~1.5 V but are stable from −2 to +1 V with a yield of 93%; the junctions comprising SAMs of **FP2** and **FP3** are stable between −2.0 to +1.5 V, with a yield of 92% and 94%, respectively (Table S6). As a comparison, junctions comprising SAMs of alkanethiols show comparable yields at a significantly narrower bias window (*e.g.*, −0.5 to +0.5 V in Fig. S7) but short at biases of around |1 V|. Intermolecular van der Waals interactions between the side chains of the 3,5-bis(trihexylsilyl)phenyl groups of **P1** and the fused porphyrin oligomers seem to effectively compensate the loss of packing density to facilitate the formation of robust SAMs.

The current density J for each SAM (*i.e.* the tunnelling current divided by the junction area, determined optically) is plotted as a function of bias voltage V in Fig. 1c, and the heat maps in Fig. 1d–f show the distribution of J/V curves from over 40 junctions for each type (see Fig. S8 for individual curves). The junctions display molecule-dependent charge-transport properties, with a prominent and unipolar clockwise hysteresis loop for **FP2** and **FP3** SAMs at positive bias. For these junctions, as the bias voltage is increased from 0 V, the current density initially rises rapidly, but then plateaus and begins to fall (displaying negative differential conductance, NDC), and, on the reverse sweep back to 0 V, it follows a lower trajectory. Whilst the effect is minimal for the porphyrin monomer **P1**, for the SAMs of **FP2** and **FP3** it leads to two distinctly different conductance states that depend on the sweep direction. For example, at 0.5 V for **FP2**, the high conductance state (HCS) sustains a current of 43 ± 6 mA cm^{-2} compared to 1.6 ± 0.4 mA cm^{-2} for the low conductance state (LCS) on the return sweep, and for **FP3** we measure 27 ± 4 mA cm^{-2} and 0.12 ± 0.03 mA cm^{-2}, respectively.

Framing the $J(V)$ behavior in the context of molecular memory and computation, we can define voltage sweeps that modulate the junction conductance as WRITE, ERASE and READ operations (Fig. 1c–f and Fig. 2a). A single triangular voltage sweep from 0 V to 1.0 V changes a junction from being in initially a HCS to a LCS, and we denote this a WRITE operation. In Fig. 2a, we plot the voltage dependence of the HCS: LCS ratio, $R_{f/b} = J(V_{forward})/J(V_{backward})$. For **FP2** SAMs, we measure $R_{f/b}$ as ~30 (max. 40) between 0–0.75 V, and for **FP3** SAMs $R_{f/b}$ is stable at ~230 (max. 350) between 0–0.6 V, with a gradual decrease to zero as the bias continued to increase, corresponding to the convergence of J/V curves at 1.5 V. In contrast, the SAMs of **P1** displayed a significantly lower $R_{f/b}$ of 1.4. At 0.5 V, the $R_{f/b}$ values for the **FP2** and **FP3** junctions are stable, and this voltage is below the threshold that generates the NDC effect. Therefore, we assign a sweep up to 0.5 V as a READ operation, as this is sufficient to determine the conductance (depending on whether a high or low current density is measured) without altering it. There is a notable asymmetry within the system: an ERASE operation, a negative voltage sweep to −2.0 V, is not sufficient to fully return the junction to the HCS in a single step. In Fig. 2b, we demonstrate that after

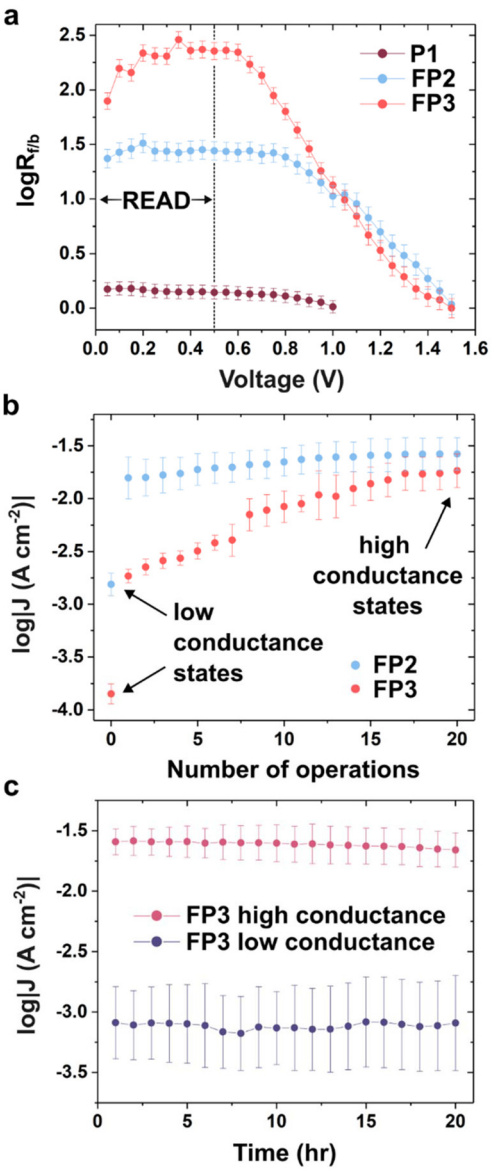

Fig. 2 (a) The ratio of current density on the forward: backward parts of a WRITE sweep to 1.5 V as a function of bias voltage, demonstrating the increase with molecular length. The vertical dashed line indicates the limit of possible READ voltages – a sweep below this voltage is reversible, enabling the current state to be read but not modified. (b) The current density measured by a READ during a sequence of ERASE operations (triangular sweep from 0 V to −2.0 V) for **FP2** and **FP3** junctions after a WRITE. (c) After initialization of an **FP3** junction in the high conductance or low conductance state the current density, measured by a READ at 0.5 V, remains stable over the course of 20 hours. (All log values are decadic.).

a WRITE, 20 ERASE operations are needed to reset the junction to the original value of the HCS, with a series of intermediate conductance states (measured by a READ after each ERASE) in between. In this scheme, operations were programmed at a rate of 10 Hz, corresponding to ramp rates of 20 (40) V s^{-1} for WRITE (ERASE), although a high $R_{f/b}$ could be maintained up to 50 Hz, as shown in Fig. S12, above this a drop is observed. A switching frequency of 50 Hz is comparable to other Au/SAM//EGaIn systems,[8,9] and may be attributed to the molecular mechanism itself, or combined resistances and capacitances within the SAM[24] and the external circuit. We also studied the stability of the HCS and LCS for an **FP3** junction, as these displayed the largest $R_{f/b}$ of the SAMs studied. Over the course of 20 hours, we found the LCS to be stable, with $J < 10^{-3.0}$ Acm^{-2} in this timeframe. A slight drop in the current density was measured for the HCS, which may be due to gradual oxidation of the thiol groups that can occur on these timescales and affect junction properties (such as rectification[25]), although the ratio, $R_{f/b}$ only decreased slightly before junction failure at 20 hours (reason unknown).

The current density increases roughly linearly with the number of ERASEs since the last WRITE, as shown in Fig. 3, where we plot 10 such cases. Altogether Fig. 3 presents the course of 210 operations (10 loops of: one WRITE operation followed by 20 ERASE operations), programmed at a rate of 10 Hz, and demonstrates that it is possible to repeatedly access a series of intermediate conductances between the LCS and HCS. This sequence is the largest number of operations (which is 420 including the READs) that we applied to a single junction, although all junctions comprising **P1**, **FP2** and **FP3** SAMs that contributed to the heat maps (Fig. 1d–f) were cycled at least 20 times, and otherwise counted as a junction failure (see Experimental section and Table S6). Overall, the set of experiments in Fig. 1–3 demonstrate that the **FP3** junctions (and to a lesser extent **FP2**) behave as memristive elements over our experimental timeframe, *i.e.*, they display both non-volatility (in retaining their conductance state even at 0 V) as well as a conductance that depends on the history of WRITE and ERASE operations.

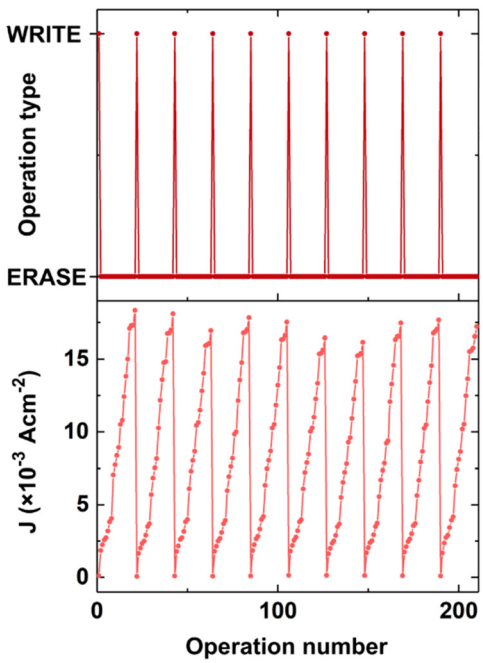

Fig. 3 A series of WRITE (to 1 V) and 20 ERASE (to −2 V) operations (applied at 10 Hz, shown in top panel) to a **FP3** junction show that a linear series of analog junction conductances are reproducibly accessible between the LCS, which is formed directly after a WRITE, and the HCS. The conductance is measured by a READ (0.5 V) after each WRITE or ERASE operation.

The length dependence of current density through molecular junctions can be parametrized by treating the molecules as a tunnel barrier, $J = J_0 e^{-\beta d}$, where d is the layer thickness or molecular length and β is a (bias-voltage dependent) property of the molecules under study. Prior to the WRITE, for the SAMs of **P1**, **FP2**, and **FP3**, we calculate a small β of 0.07 ± 0.01 $Å^{-1}$ at 0.5 V (*cf.* for alkane thiols, we measure β = 0.6 ± 0.01 $Å^{-1}$, see Fig. S7). There are several reported causes of low β values,[26] such as increasing diradical character with length,[27] or a decoupling between the molecule orbitals and electrode states.[28] The small β measured for **P1**, **FP2**, and **FP3** SAMs is consistent with single-molecule conductance measurements[12,15] and attributable to the reduction of HOMO–LUMO gap with molecular length as predicted by DFT calculations (Fig. S13 and ref. 15) and shown by electrochemical measurements (Table S1). The consequence of the reduced gap is to lower the energy difference, ΔE, between the dominant transport orbital (the HOMO[15]) and the electrode work functions (*i.e.* the height of the tunnel barrier), with increasing oligomer length. The attenuation behavior changes markedly after a WRITE, with β increasing to 0.38 ± 0.03 $Å^{-1}$, suggesting the operation has increased ΔE for **FP2** SAMs and, to a greater extent, **FP3** SAMs (the current density through **P1** is unchanged, there is no hysteresis).

We also measured the temperature dependence of transport through **FP3** SAMs between 20 °C and 45 °C by mounting the sample on a resistive heater and measuring the temperature on the Au^{TS} surface near to the junction. Prior to the WRITE, the current density at 0.5 V is independent of temperature, and coupled with the low β, this is consistent with near-resonant elastic tunnelling as the dominant transport mechanism. After the WRITE, and in line with the onset of the NDC and hysteresis loop, the current density through **FP3** SAMs drops by several orders of magnitude (as previously discussed), and also becomes highly temperature dependent, with an activation energy of 0.96 eV calculated from an Arrhenius-type plot (Fig. 4b, full temperature-dependent sweeps are in Fig. S11). Again, this is consistent an increase in ΔE for these junctions – post-WRITE, the elastic transport channel for **FP3** SAMs is no longer an efficient transport pathway, and the low residual current of the LCS is mediated by inelastic tunneling.

These observations suggest a different mechanism is responsible for conductance switching than that reported in single-molecule conductance studies on the same (or similar)

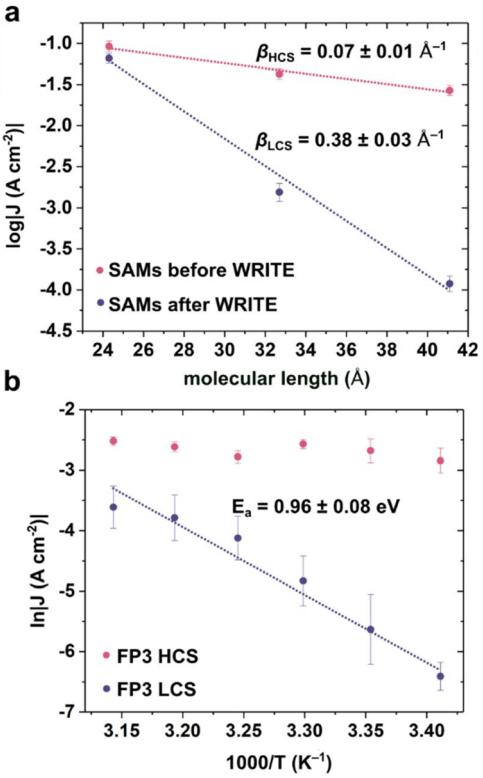

Fig. 4 (a) The molecular-length dependence of the current density before and after a WRITE operation. (b) The current density of the **FP3** HCS and LCS measured as a function of temperature. Values in (a) and (b) are both determined by a READ at 0.5 V. The errors reported with the fitted values are one standard deviation.

compounds between gold contacts.[14,15] In these single-molecule experiments the suggested switching mechanism involves a changing occupation of the HOMO−1 (accessible due to the small orbital spacings within fused porphyrin oligomers), which is very weakly coupled to the electrodes, following a theoretical model proposed by Migliore and Nitzan[29,30] that has been used to explain low-temperature single-molecule conductance switching in other redox-active molecules.[31,32] The oxidized molecule has higher conductance but is only metastable in the junction, relaxing to the (neutral) low-conductance state in seconds. In contrast, the Au/SAM//EGaIn junctions studied here are already in a high conductance state upon formation and a positive bias is required to transform them to the LCS. Furthermore, both states are stable for hours, a timescale that would require an extremely small coupling to the HOMO−1 with the model above, and a series of intermediate conductance values are accessible.

Previous studies that have shown only a small fraction of the molecules (as few as 10^{-4}) within the optically determined junction area are responsible for conduction in most Au/SAM//EGaIn junctions.[33] A possible mechanism of switching in our junctions involves bias-induced oxidation during a WRITE operation of molecules that are not strongly coupled to both electrodes, and that do not carry the tunnelling current. A net build-up of positive charge during the WRITE effectively gates transport through the conductive neutral molecules, increasing ΔE and decreasing the overall conductance (see Fig. S14 and S15 for a scheme and simulation of the proposed mechanism). The charged molecules are stabilized through relaxation of the electrostatic environment, for example through ion-induced dipole interactions within the SAMs. These attractive interactions increase with molecular length and polarizability (which increases with size and a decreasing HOMO–LUMO gap for a homologous series of molecules[34]), and therefore follow the trend of redox activity: **FP3** > **FP2** > **P1**, in line with the prominence of the observed hysteresis. This is a mechanism with similarities to those invoked in other SAM or large-area molecular junctions that display hysteresis, where charging followed by intermolecular stabilization through *e.g.*, dimerization and ion migration in SAMs,[8] or through disproportionation in thicker films[35] gives different conductance states that are stable over timescales of hours. After partial SAM oxidation by the WRITE, each ERASE operation reduces a fraction of the cations back to neutral form, giving a stepwise decrease in ΔE and the analog conductance increase we observe with number of operations.

Conclusions

We have demonstrated that fused porphyrins formed into SAM junctions between gold and EGaIn electrodes show molecular-length-dependent charge transport behavior. The fused dimer and trimer (**FP2** and **FP3**) junctions behave like memristors, *i.e.*, they display current hysteresis *vs.* voltage and have associated conductance states that are stable for up to 20 hours for **FP3**. Furthermore, through different combinations of WRITE and ERASE operations, it is possible to tune the device conductance, not just between a high and a low state, but a series of intermediate values which is an important property for analog computing applications. An exploration of the limits of junctions – in terms of switching performance and stability – will necessitate moving away from liquid metal electrodes towards static device-like junction configurations, such as a crossbar arrays, and incorporating encapsulating layers as part of their structure.[36]

Experimental

Preparation of self-assembled monolayers (SAMs)

The SAMs of CnSH ($C_nH_{2n+1}SH$, n = 8, 10, 12, 14 and 16) for control experiments were prepared by incubating freshly cleaved 1 × 1 cm^2 Au^{TS} substrates for 24 h in 4 mL of 2 mM solution of CnSH in pure ethanol under inert atmosphere at room temperature. The Au^{TS} substrates were fabricated using the method reported in literature.[37] In short, we deposited a 100 nm-thick Au film on atomically flat Si wafer which served as template by thermal evaporation. The Si wafer was then glued to 1 × 1 cm^2 glass supports by applying an optical

adhesive (Norland 61) and cured under UV light. The Au surface against the Si wafer was exposed by mechanically lifting the glass support and the substrates were used immediately for sample preparation. The samples were first rinsed gently with pure ethanol (3 mL), and we removed the residual ethanol by gently blowing the samples with dry N_2. The SAMs of fused porphyrin tapes (*i.e.*, **P1**, **FP2** and **FP3**) were prepared by incubating cleaved 1 × 1 cm^2 Au^{TS} substrates for 24 h in 2 mL of 0.02–0.05 mM solution of fused porphyrin tapes in anhydrous toluene under inert atmosphere at room temperature. The samples were then rinsed gently with toluene (3 mL), and we removed the residual toluene by gently blowing the samples with dry N_2.

AFM measurements

All samples, including bare Au^{TS} substrates and SAMs, studied in this work were characterized on a JPK Instruments NanoWizard 3 model operated in tapping mode. The measurements were performed with a SCOUT 350 RAl probe (resonant frequency 350 kHz, spring constant 42 N m^{-1}, NuNano) to characterize the surface morphology of the samples at a scan rate of 0.7 Hz and 512 samples per line, followed by data analysis with Gwyddion 2.58.

XPS measurements

XPS measurements were performed using a Thermo Scientific K-Alpha XPS equipped with a microfocused monochromated Al X-ray source (Kα, 1486.6 eV). A Lorentzian–Gaussian fit with Shirley background was made to the peaks to obtain their intensities.

EGaIn measurements

Electrical measurements with EGaIn, as well as sample preparation and handling, were performed under ambient conditions. During the measurements, the sample was grounded and the EGaIn electrode was biased. All sweeps have a fixed step size of 0.05 V and varied rates (*i.e.*, 0.01–1 s time intervals between two steps). For reproducing the tunneling decay coefficient on SAMs of alkanethiols, a total of five trace/retrace cycles were recorded for each junction; for characterizing the charge-transport properties of SAMs of fused porphyrin tapes, a total of 20–40 trace/retrace cycles (including the WRITE-READ-ERASE cycles) were recorded for each junction, and shorts occurring during the measurement (short upon contact with a bias of 0.5 V or during the cycle) were counted as failure of the junction.

J/*V* data processing and analysis

Data were acquired as described and then processed to produce histograms of log|*J*| for each value of *V*. Gaussian fits (using a least-squares fitting routine) were used to determine the averages values, μ, which were plotted against molecular length (in Å or number of carbons) to calculate β values reported in Fig. 4. This analysis mitigates the influence of measurement artifacts and separates them from the influence of defects in the tunneling junctions,[38] and the β values becomes meaningful for comparison against other experimental platforms. We used this methodology of analysing histograms of log|*J*| to construct the *J*/*V* curves shown in the main text and SI. The histogram of the raw *J*/*V* data and Gaussian fits are shown in Fig. S9 and Fig. S10, examples of unprocessed *J*/*V* curves are shown in Fig. S8.

Water contact angle

Equilibrium contact angles were obtained by applying 1 μL water droplets on bare Au^{TS} or SAM-modified substrates using the sessile drop method. The contact angles were measured on two samples, at three different locations per sample, and the results were averaged with standard deviation as the error bars.

Author contributions

X. Q.: conceptualization, data curation, formal analysis, investigation, resources, visualization, writing – original draft, writing – review & editing. J. R. D.: formal analysis, investigation, writing – review & editing. G. A. D. B.: conceptualization, funding acquisition, project administration, resources, writing – review & editing. H. L. A:. conceptualization, funding acquisition, project administration, resources, supervision, writing – original draft, writing – review & editing. J. O. T.: conceptualization, investigation, project administration, supervision, visualization, writing – original draft, writing – review & editing.

Conflicts of interest

There are no conflicts to declare.

Data availability

The data supporting this article are included in the main text and the SI. Supplementary information: synthesis, self-assembled monolayer characterization, additional charge transport measurements, DFT calculations, potential mechanism. See DOI: **https://doi.org/10.1039/d5nr02773j**.

Acknowledgements

X. Q., J. O. T., H. L. A. and G. A. D. B. acknowledge the EPSRC QuEEN Programme Grant (EP/N017188/1) and J. O. T., H. L. A., and G. A. D. B. acknowledge support through the EPSRC NSNF Platform Grant (EP/R029229/1). H. L. A. also acknowledges the EPSRC QMol Programme Grant (EP/X026876/1). We thank Dr Philip Holdway at the University of Oxford, UK, for his help with XPS measurements, and Dr He Zhu at the University of Oxford, UK, for her helpful suggestion on the synthesis of the monomer.

References

1 J. R. Heath, *Annu. Rev. Mater. Res.*, 2009, **39**, 1–23.
2 D. B. Strukov, G. S. Snider, D. R. Stewart and R. S. Williams, *Nature*, 2008, **453**, 80–83.
3 P. Mannocci, M. Farronato, N. Lepri, L. Cattaneo, A. Glukhov, Z. Sun and D. Ielmini, *APL Mach. Learn.*, 2023, **1**, 010902.
4 Y. van de Burgt, A. Melianas, S. T. Keene, G. Malliaras and A. Salleo, *Nat. Electron.*, 2018, **1**, 386–397.
5 D. Sharma, S. P. Rath, B. Kundu, A. Korkmaz, H. S, D. Thompson, N. Bhat, S. Goswami, R. S. Williams and S. Goswami, *Nature*, 2024, **633**, 560–566.
6 J. Li, S. Hou, Y.-R. Yao, C. Zhang, Q. Wu, H.-C. Wang, H. Zhang, X. Liu, C. Tang, M. Wei, W. Xu, Y. Wang, J. Zheng, Z. Pan, L. Kang, J. Liu, J. Shi, Y. Yang, C. J. Lambert, S.-Y. Xie and W. Hong, *Nat. Mater.*, 2022, **21**, 917–923.
7 J. Lee, H. Chang, S. Kim, G. S. Bang and H. Lee, *Angew. Chem., Int. Ed.*, 2009, **48**, 8501–8504.
8 Y. Han, C. Nickle, Z. Zhang, H. P. A. G. Astier, T. J. Duffin, D. Qi, Z. Wang, E. del Barco, D. Thompson and C. A. Nijhuis, *Nat. Mater.*, 2020, **19**, 843–848.
9 Y. Wang, Q. Zhang, H. P. A. G. Astier, C. Nickle, S. Soni, F. A. Alami, A. Borrini, Z. Zhang, C. Honnigfort, B. Braunschweig, A. Leoncini, D.-C. Qi, Y. Han, E. del Barco, D. Thompson and C. A. Nijhuis, *Nat. Mater.*, 2022, **21**, 1403–1411.
10 S. Kumar, M. Merelli, W. Danowski, P. Rudolf, B. L. Feringa and R. C. Chiechi, *Adv. Mater.*, 2019, **31**, 1807831.
11 G. Sedghi, L. J. Esdaile, H. L. Anderson, S. Martin, D. Bethell, S. J. Higgins and R. J. Nichols, *Adv. Mater.*, 2012, **24**, 653–657.
12 E. Leary, B. Limburg, A. Alanazy, S. Sangtarash, I. Grace, K. Swada, L. J. Esdaile, M. Noori, M. T. González, G. Rubio-Bollinger, H. Sadeghi, A. Hodgson, N. Agraït, S. J. Higgins, C. J. Lambert, H. L. Anderson and R. J. Nichols, *J. Am. Chem. Soc.*, 2018, **140**, 12877–12883.
13 G. Sedghi, V. M. García-Suárez, L. J. Esdaile, H. L. Anderson, C. J. Lambert, S. Martín, D. Bethell, S. J. Higgins, M. Elliott, N. Bennett, J. E. Macdonald and R. J. Nichols, *Nat. Nanotechnol.*, 2011, **6**, 517–523.
14 J.-R. Deng, M. T. González, H. Zhu, H. L. Anderson and E. Leary, *J. Am. Chem. Soc.*, 2024, **146**, 3651–3659.
15 E. Leary, G. Kastlunger, B. Limburg, L. Rincón-García, J. Hurtado-Gallego, M. T. González, G. R. Bollinger, N. Agrait, S. J. Higgins, H. L. Anderson, R. Stadler and R. J. Nichols, *Nanoscale Horiz.*, 2021, **6**, 49–58.
16 J. Woo and S. Yu, *IEEE Nanotechnol. Mag.*, 2018, **12**, 36–44.
17 J. M. Tour, L. Jones II, D. L. Pearson, J. J. S. Lamba, T. P. Burgin, G. M. Whitesides, D. L. Allara, A. N. Parikh and S. Atre, *J. Am. Chem. Soc.*, 1995, **117**, 9529–9534.
18 D. S. Seferos, D. A. Banach, N. A. Alcantar, J. N. Israelachvili and G. C. Bazan, *J. Org. Chem.*, 2004, **69**, 1110–1119.
19 K. H. A. Lau, C. Huang, N. Yakovlev, Z. K. Chen and S. J. O'Shea, *Langmuir*, 2006, **22**, 2968–2971.
20 H. Valkenier, E. H. Huisman, P. A. van Hal, D. M. de Leeuw, R. C. Chiechi and J. C. Hummelen, *J. Am. Chem. Soc.*, 2011, **133**, 4930–4939.
21 J. C. Love, D. B. Wolfe, R. Haasch, M. L. Chabinyc, K. E. Paul, G. M. Whitesides and R. G. Nuzzo, *J. Am. Chem. Soc.*, 2003, **125**, 2597–2609.
22 T. Kondo, M. Yanagida, K. Shimazu and K. Uosaki, *Langmuir*, 1998, **14**, 5656–5658.
23 R. C. Chiechi, E. A. Weiss, M. D. Dickey and G. M. Whitesides, *Angew. Chem., Int. Ed.*, 2008, **47**, 142–144.
24 C. S. S. Sangeeth, A. Wan and C. A. Nijhuis, *J. Am. Chem. Soc.*, 2014, **136**, 11134–11144.
25 G. D. Kong and H. J. Yoon, *J. Electrochem. Soc.*, 2016, **163**, G115–G121.
26 H. J. Lee, S. J. Cho, H. Kang, X. He and H. J. Yoon, *Small*, 2021, **17**, 2005711.
27 T. Stuyver, T. Zeng, Y. Tsuji, P. Geerlings and F. De Proft, *Nano Lett.*, 2018, **18**, 7298–7304.
28 B. Q. Xu, X. L. Li, X. Y. Xiao, H. Sakaguchi and N. J. Tao, *Nano Lett.*, 2005, **5**, 1491–1495.
29 A. Migliore and A. Nitzan, *J. Am. Chem. Soc.*, 2013, **135**, 9420–9432.
30 A. Migliore and A. Nitzan, *ACS Nano*, 2011, **5**, 6669–6685.
31 F. Schwarz, G. Kastlunger, F. Lissel, C. Egler-Lucas, S. N. Semenov, K. Venkatesan, H. Berke, R. Stadler and E. Lörtscher, *Nat. Nanotechnol.*, 2016, **11**, 170–176.
32 F. Schwarz, M. Koch, G. Kastlunger, H. Berke, R. Stadler, K. Venkatesan and E. Lörtscher, *Angew. Chem., Int. Ed.*, 2016, **55**, 11781–11786.
33 F. C. Simeone, H. J. Yoon, M. M. Thuo, J. R. Barber, B. Smith and G. M. Whitesides, *J. Am. Chem. Soc.*, 2013, **135**, 18131–18144.
34 S. Góger, L. M. Sandonas, C. Müller and A. Tkatchenko, *Phys. Chem. Chem. Phys.*, 2023, **25**, 22211–22222.
35 S. Goswami, S. P. Rath, D. Thompson, S. Hedström, M. Annamalai, R. Pramanick, B. R. Ilic, S. Sarkar, S. Hooda, C. A. Nijhuis, J. Martin, R. S. Williams, S. Goswami and T. Venkatesan, *Nat. Nanotechnol.*, 2020, **15**, 380–389.
36 Q. Xia and J. J. Yang, *Nat. Mater.*, 2019, **18**, 309–323.
37 E. A. Weiss, G. K. Kaufman, J. K. Kriebel, Z. Li, R. Schalek and G. M. Whitesides, *Langmuir*, 2007, **23**, 9686–9694.
38 W. F. Reus, C. A. Nijhuis, J. R. Barber, M. M. Thuo, S. Tricard and G. M. Whitesides, *J. Phys. Chem. C*, 2012, **116**, 6714–6733.